Title

Continuous, long-term, high-frequency thermal imaging of vegetation: Uncertainties and recommended best practices

Permalink

https://escholarship.org/uc/item/9fz9v32c

Authors

Aubrecht, Donald M
Helliker, Brent R
Goulden, Michael L
et al.

Publication Date

2016-11-01

DOI

10.1016/j.agrformet.2016.07.017

Agricultural and Forest Meteorology 228–229 (2016) 315–326

Contents lists available at ScienceDirect

Agricultural and Forest Meteorology

journal homepage: www.elsevier.com/locate/agrformet

Continuous, long-term, high-frequency thermal imaging of vegetation: Uncertainties and recommended best practices

Donald M. Aubrecht[a,*], Brent R. Helliker[b], Michael L. Goulden[c], Dar A. Roberts[d], Christopher J. Still[e], Andrew D. Richardson[a]

[a] Department of Organismic and Evolutionary Biology, Harvard University, Cambridge, MA 02138, USA
[b] Department of Biology, University of Pennsylvania, Philadelphia, PA 19104, USA
[c] Department of Earth System Science, University of California, Irvine, CA 92697, USA
[d] Department of Geography, University of California, Santa Barbara, CA 93106, USA
[e] Department of Forest Ecosystems and Society, Oregon State University, Corvallis, OR 97331, USA

ARTICLE INFO

Article history:
Received 20 April 2016
Received in revised form 19 July 2016
Accepted 19 July 2016
Available online 1 August 2016

Keywords:
Thermal infrared
Canopy temperature
Camera
Forest
Phenology
Microbolometer

ABSTRACT

Leaf temperature is an elementary driver of plant physiology, ecology and ecosystem productivity. Individual leaf temperature may deviate strongly from air temperature, and may vary throughout the canopy. Measurements of leaf temperature, conducted at a high spatial and temporal resolution, can improve our understanding of leaf water loss, stomatal conductance, photosynthetic rates, phenology, and atmosphere-ecosystem exchanges. However, continuous high-resolution measurement of leaf temperature outside of a controlled environment is difficult and rarely done. Here, thermal infrared cameras are used to measure leaf temperatures. We describe two long-term field measurement sites: one in a temperature deciduous forest, and the other in a subalpine conifer forest. The considerations and constraints for deploying such cameras are discussed and the temperature errors are typically +/−1 °C or smaller ($\sigma = 0.60\,^{\circ}$C, $2\sigma = 1.20\,^{\circ}$C). Lastly, we compare leaf temperature by species and height at hourly to multi-seasonal timescales and show that on average, leaf temperature is warmer than air temperature in a temperate forest. Leaf temperature can be uniform or heterogeneous across a scene, depending on canopy structure, leaf habit, and meteorology. With this data, we verify that leaf temperature follows classic expectations, yet exhibits noteworthy departures that require additional study and theoretical consideration.

1. Introduction

The effect of temperature on photosynthesis and transpiration by plant canopies is of fundamental importance to plant evolution, productivity, and distribution (Long and Woodward, 1988; Schimper, 1903; von Humboldt and Bonpland, 1807; Walter et al., 1975). Variations in canopy temperature directly affect leaf-water loss and photosynthetic rates, impacting tree budgets and ecosystem-scale exchanges of water, carbon, and energy. Leaf temperature affects photosynthesis by changing cell membrane fluidity, enzyme reaction kinetics, diffusion constants and dissolution of CO_2 and O_2, which control the ratio of photorespiration to photosynthesis (Lambers et al., 1998). Though we have general understanding of the factors that influence leaf temperature (Gates, 1980, 1968, 1964), we lack high quality, high frequency, long-term data with which to validate and improve leaf temperature simulation models. This lack of data has largely been due to the logistical constraints on recording leaf temperatures in a natural, uncontrolled environment.

Previously, measuring leaf temperature in the field has been accomplished by two techniques: (1) affixing fine-wire thermocouples to vegetation, or (2) using thermal infrared (TIR) thermometers. Thermocouple measurements require vigilance to ensure the thermocouples remain attached to the vegetation and necessitate a Herculean effort to obtain statistically significant measures of total canopy temperature and how leaf temperature varies throughout the canopy (Miller, 1972, 1971). Therefore, thermocouples limit data to small sample numbers over relatively short time periods. Likewise, TIR thermometer measurements suffer

---

* Corresponding author at: 138 HUH, 22 Divinity Avenue, Cambridge, MA 02138, USA.

E-mail addresses: aubrecht@oeb.harvard.edu (D.M. Aubrecht), helliker@sas.upenn.edu (B.R. Helliker), mgoulden@uci.edu (M.L. Goulden), dar@geog.ucsb.edu (D.A. Roberts), chris.still@oregonstate.edu (C.J. Still), arichardson@oeb.harvard.edu (A.D. Richardson).

http://dx.doi.org/10.1016/j.agrformet.2016.07.017

from a lack of spatial and/or temporal resolution. Field mountable thermometers (also known as infrared radiometers) offer a "blind" approach, which integrates thermal signals from target and non-target objects (e.g. branches and soil) into a single value for the field-of-view. Point-and-shoot, portable TIR thermometers (such as the TG165 spot camera, FLIR Systems, Inc.) lack temporal resolution, giving sparse data on a rapidly varying quantity. It is not feasible to record accurate and long-term, continuous measurements of leaf and canopy temperature with either the thermocouple or infrared thermometer approach.

Within the past two decades, thermal infrared cameras have been developed with the robustness, power specifications, pixel resolution, and sensitivity to enable continuous monitoring of canopy temperatures across an entire growing season (Kruse and Skatrud, 1997; Vollmer and Möllmann, 2010). These sensors are also small and affordable enough to deploy to field sites. Recent work with thermal cameras has demonstrated the power to measure species-specific responses to leaf energy balance, but did not capitalize on the continuous monitoring capability of these instruments, nor did the work assess measurement error (Leuzinger and Körner, 2007; Leuzinger et al., 2010; Reinert et al., 2012; Scherrer et al., 2011). Additional work has utilized thermal cameras for characterization of stomatal conductance and closure, irrigation schedules, and plant stress, but focused exclusively on laboratory or crop field environments where some external factors can be controlled, and also did not take advantage of the continuous monitoring capabilities of the technology (Ballester et al., 2013; Berger et al., 2010; Grant et al., 2006; Jones, 2004, 1999; Jones et al., 2009).

There are three goals for this work. First, we quantify the accuracy of continuous thermal infrared imaging in natural, forested settings. We characterize the errors in image-derived temperatures, describe the accuracy with which environmental and vegetation parameters must be known, and show that sensor noise has a minimal impact on the temporal and spatial variation of pixels in an image. Secondly, we suggest best practices for acquiring TIR image data, and create software for correcting interferences in large datasets of images. Finally, we use these new data and tools to explore the thermal signatures of deciduous and evergreen vegetation on timescales ranging from seconds to multiple seasons.

2. Materials and methods

2.1. Site descriptions

Our primary field site is the 40 m tall "Barn Tower" (42.5353°N 72.1899°W) at the Harvard Forest, 110 km west of Boston, MA. The tower is surround by mixed forest stands dominated by red oak (*Quercus rubra* L.), red maple (*Acer rubrum* L.), and white pine (*Pinus strobus* L.). We have mounted two thermal infrared cameras atop the tower: a model A655sc (FLIR Systems, Inc., 640 × 480 pixel resolution, 45° FOV), and a model A325sc (FLIR Systems, Inc., 320 × 240 pixel resolution, 6° FOV). The cameras point north, are inclined 20–30° below the horizon, and are arranged such that the FOV of the A325 is a zoomed-in region of the A655 FOV. Images are acquired continuously every 15 min by FLIR's ExaminIR software running on fanless industrial computers (Neousys POC-100, Logic Supply, Inc.) at the base of the tower and connected to the cameras via Ethernet. We have also recorded several days of images at one-second intervals.

Mounted atop the same tower, observing the same canopy are: two VIS-NIR networked digital cameras (StarDot NetCam SC), one VIS-NIR hyperspectral camera (Surface Optics Corporation SOC710), a 4-channel net radiometer (Kipp & Zonen CNR4), a dual temperature/relative humidity probe (Vaisala HMP35c), a sunshine sensor (Delta-T Devices BF5), and an eddy-covariance flux system (LI-COR LI-7200, LI-7550 controller, 7200-101 flow module). These instruments provide measurements necessary for correcting interferences in the images recorded by the FLIR cameras and for interpreting differences between canopy and air temperature.

A matte black painted copper plate (6″ × 6″ × 0.075″, emissivity = 0.985) is mounted in the canopy with a copper-constantan thermocouple affixed to its back. The plate is visible in the FOV of both thermal cameras, and the thermocouple is logged continuously at rates of 0.1–5 Hz, depending on season. In addition, 12 fine-wire thermocouples were affixed to the abaxial surface of leaves in an oak canopy within the FOV of the cameras (approximately 33 m from the cameras) for 25–27 June 2013. The thermocouples were recorded as 30 s mean values.

We have deployed a similar instrument package to the 26 m tall Ameriflux tower (40.0329°N 105.5464°W) at the University of Colorado's Mountain Research Station on Niwot Ridge, 40 km west of Boulder, CO. The tower is surround by mix of evergreen needleleaf species: lodgepole pine (*Pinus contorta* Douglas ex Loudon), Engelmann spruce (*Picea engelmannii* Parry ex Engelm.), and subalpine fir (*Abies lasiocarpa* (Hook.) Nutt.). We have mounted an A655sc camera (FLIR Systems, Inc., 640 × 480 pixel resolution, 45° FOV) near the top of the tower, pointed east and inclined about 30° below the horizon. Supporting measurements are made similar to the Harvard Forest instrumentation, and image acquisition is performed by FLIR's ResearchIR software running on a fanless industrial computer mounted on the tower. Visible images of the canopy at Harvard Forest and Niwot Ridge are provided in Supplementary Fig. S1.

2.2. Camera-canopy distance

Accurate temperature measurements with thermal cameras require knowing the distance between camera and target object so that atmospheric attenuation of the thermal signal can be calculated. For the A325 camera with the 6° lens, this is straightforward, since the narrow angle lens means that the entire field-of-view is approximately the same distance from the camera. As deployed, this distance is 33 m, measured by laser range finder, and objects within the FOV vary in distance to the camera by less than 2 m.

Determining camera-canopy distance is more challenging for the A655 cameras, since the FOV encompasses much more. As deployed, the A655 FOV include tree crowns as close as 10 m and as far as 200 m. While a rudimentary distance map for each sensor array could be generated by hand, we developed an optimized approach using digital photographs and structure from motion software to generate a 3D pointcloud of each study area and then re-render the camera scene to create a distance map for the sensor.

Briefly, low-altitude, high-resolution digital images of the Harvard Forest site were taken with 25–50% overlap between images. These images, along with coordinates and elevations of known ground control points were loaded into PhotoScan (Agisoft LLC) to calculate an accurate, 3D pointcloud of the canopy (Dandois, 2014). A similar pointcloud was generated in PhotoScan for Niwot Ridge using images taken from multiple heights and look angles on the tower. Then, each pointcloud was analyzed by a custom script to re-render each thermal camera scene. The script projects the camera pixel array onto the 3D pointcloud from the vantage point of the camera, using the camera orientation, sensor pixel dimensions, and lens FOV, and finds the pointcloud point in each pixel's solid angle projection that is closest to the camera. This point is assumed to be the one each pixel "sees", and its color is assigned to that pixel in the array. In this way, a color rendering of the visible scene is produced and can be compared to the physical locations of the tree crowns in the thermal FOV. Once the rendered scene is verified by visual assessment, a distance is assigned to each pixel, according to the coordinates of point in the pointcloud used for that pixel. Empty pixels in the distance map are filled using values interpolated from nearest neighbor pixels. The resulting distance map is then verified by laser rangefinder to measure distances between the camera and canopy features in the FOV. The distance map is accurate within +/−1 m of the laser rangefinder measurements (standard deviation of differences between pointcloud and rangefinder = 0.6 m). For all canopy data in this paper, images are corrected using these distance maps.

2.3. *Sensitivity analysis*

We explore the sensitivity of corrected pixel temperature to measurable parameters that characterize major interferences and establish the measurement accuracy required for each parameter. Three images from Harvard Forest are chosen to span the range of temperatures pertinent to vegetation: a cold image (−20–0 °C), a warm image (10–30 °C), and a hot image (20–40 °C). Each image is first processed by the analysis code using the true environmental parameters measured at the time the image was recorded. This produces the true temperature value for each pixel. The images are then reprocessed by the analysis code, stepping through a matrix of parameter values in the following ranges: emissivity = 0.8–0.99, distance = 0–150 m, air temperature = −40–60 °C, relative humidity = 0–100%, reflected object temperature = −50–100 °C.

For each combination of parameter values, temperature error from the true value is calculated and stored. Error is calculated as the mean difference between the minimum and maximum temperatures of the true image and the minimum and maximum temperatures produced by the test parameter combination. Surface plots of error as a function of parameter value are then produced for different combinations of fixed and free parameters. Fixed parameters are held at their true value for each image. In one set of plots, emissivity, distance, and reflected temperature are held fixed, while air temperature and relative humidity vary across their ranges. In the second set of plots, air temperature and relative humidity are fixed, while the other parameters vary.

2.4. *Sensor noise*

Spatial and temporal frequency response of the TIR camera sensor was characterized to establish noise limits on data measured and answer the question: in an uncontrolled natural environment, do the patterns in an object's TIR temperature over time and across its surface correspond to real variation in the object's true temperature? To test this, a rectangular plastic trashcan, painted matte black (to give a high emissivity surface) and filled with water (to maximize thermal inertia) was positioned to fill the camera's FOV. Images were taken with an A325 camera and 15° lens installed in the same weatherproof enclosure used at the tower field sites. Data were recorded at night, outdoors, with clear sky and low humidity, to minimize interferences. Under those conditions, all pixels in the sensor array should record identical temperatures, and differences are attributable to sensor noise. Images were acquired at one-second intervals for sixty minutes, and processed in MATLAB.

Frequency analysis of patterns in the thermal signals was performed using Fourier transforms in one and two dimensions, depending on the input signal. A one-dimensional Fourier transform is the mathematical operation by which a time domain signal (such as temperature versus time) is converted to the frequency domain. A power spectrum is the plot of squared amplitude versus frequency. In this manner, the frequency components contributing to the finite temporal signal are identified: dominant frequencies in the temporal signal have higher power, while frequencies with low power contribute little information to the temporal signal.

In two-dimensions, the Fourier transform converts spatial patterns in an image to spatial frequencies. Akin to the one-dimensional Fourier transform, plotting the two-dimensional power spectrum shows the spatial frequencies that contribute to the input image. The vector between the origin of the two-dimensional power spectrum plot and any point defines the direction (vector direction) and frequency (vector magnitude) for the power amplitude plotted at that point (Gonzalez et al., 2009; Kusse and Westwig, 1998). Dominant spatial frequencies have greater power amplitudes than spatial frequencies that contribute little information.

To determine the temporal noise response, temperature versus time for each pixel in the sensor array was generated from the image series, the mean of each pixel timetrace subtracted off, and the resulting signal Fourier transformed using the standard MATLAB fft function. A plot of the power spectrum from the Fourier transform results was used to identify contributing frequencies.

The spatial response of the sensor was determined in two ways. First, each thermal image frame had its mean temperature subtracted off and the signal of temperature difference from image mean versus time was created for each pixel. This temperature difference signal for each pixel was then correlated to the center pixel and the correlation coefficient plotted in each pixel's position, producing a two dimensional plot that shows how temperature changes of each pixel correlate with the center, and hence, a measure of pixel–pixel noise interactions. Second, each frame in the image sequence was transformed using the standard MATLAB fft2 function to produce a 2D power spectrum. These power spectra were averaged together to yield a mean spatial frequency power spectrum for the sensor, to deduce whether or not small spatial features are attributable to sensor noise.

3. Theory

3.1. *Principles of thermal imaging*

Thermal cameras are analogous to monochrome digital cameras: each pixel in the sensor records a digital number that represents the light intensity it receives. However, thermal cameras are sensitive to energy in a different part of the electromagnetic spectrum than normal digital cameras: TIR cameras only respond to energy with wavelength 8–14 μm. This band is different from the other infrared bands commonly used in remote sensing of vegetation: near infrared (NIR = 0.75–1.4 μm) or short-wave infrared (SWIR = 1.4–3 μm), neither of which can be used to measure physiologically relevant temperatures. In this way, TIR cameras provide information about vegetation that cannot be attained from standard digital cameras or VIS-IR spectroradiometers (Jensen, 2000).

All objects with temperatures above absolute zero emit energy in the thermal band, with the spectral radiance, I, following Planck's Law (Minkina and Dudzik, 2009; Vollmer and Möllmann, 2010):

$$I_\lambda(T) = \frac{2hc^2}{\lambda^5}\frac{1}{e^{\frac{hc}{\lambda k_B T}} - 1} \quad (1)$$

T is the object's temperature, h is the Planck constant ($h = 6.626 \times 10^{-34}$ m^{2}kg/s), c is the speed of light ($c = 3 \times 10^8$ m/s), λ is the wavelength of the radiation, and k_B is the Boltzmann constant ($k_B = 1.3806 \times 10^{-23}$ m^{2}kg/(s^{2}K)). The warmer an object is, the more energy it emits in the TIR band, and the shorter the wavelength for the peak of its emission spectrum, λ_{max}, approximated by Wein's Displacement Law (Minkina and Dudzik, 2009; Vollmer and Möllmann, 2010):

$$\lambda_{max} = \frac{b}{T} \quad (2)$$

where T is the object temperature, and b is Wein's displacement constant ($b = 2.8978 \times 10^{-3}$ m K).

Objects are also able to absorb or reflect thermal energy emitted by their surroundings. The balance between absorption and reflec-

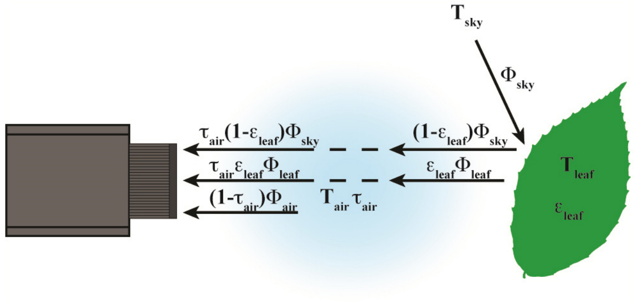

Fig. 1. Schematic of total thermal energy recorded by a thermal infrared camera. The temperature signal from vegetation (T_{leaf}) is contaminated by thermal reflections of the sky and surroundings (Φ_{sky}), signal attenuation by water vapor between the vegetation and camera (τ_{air}), and addition of thermal energy by water vapor in the air (Φ_{air}).

tion is characterized by the emissivity of an object, ε, which is a function of its surface properties. Objects that are good at absorbing thermal energy will increase their temperature and reemit some of the energy, and as such have an emissivity near one. Objects that primarily reflect energy have an emissivity near zero (Gates, 1980). Multiple interactions and reflections impact the total energy the TIR camera records for a target object (Minkina and Dudzik, 2009; Vollmer and Möllmann, 2010) and are summarized in Fig. 1. In order to accurately determine a target object's surface temperature, each of the major interferences needs to be properly accounted for when processing the raw data from the camera sensor.

There is a cascading chain of reflections and absorptions of thermal energy, Φ, that affect the signal recorded by the imaging sensor. The center path in Fig. 1 shows the thermal energy emitted by a leaf being attenuated by water vapor in the air column between the vegetation and the camera. This attenuation is characterized by the transmittance of the air column, τ_{air}. The upper path in Fig. 1 shows thermal energy from the sky and surroundings reflected by the leaf and then attenuated by water vapor in the air column. The energy contributions to this reflected energy are determined by the view factor of the leaf (Campbell and Norman, 1998): the objects that are geometrically capable of being reflected from the leaf (i.e. sky, other branches, the ground, and the camera). Finally, the lower path shows the energy contribution from the air column. Since the air is warmer than absolute zero, it, too, emits thermal energy that the camera records.

In the field, where thermal cameras are mounted tens of meters away from vegetation and there is no control of air temperature, humidity, or the temperature of other objects, this chain can have a substantial impact on the perceived temperature of the vegetation. These concerns apply not only to TIR camera sensors, but also to measurements made by TIR thermometers and the outgoing longwave sensors on net radiometers. In practice, the three most significant contributions to the perceived temperature of an object are: (1) emissivity of the target object, (2) temperature of surrounding objects or sky that are reflected by the target object, and (3) attenuation of signal from the target object and thermal emission of water vapor present in the air column between the object and camera. Accounting for these interferences and their relative magnitudes will be discussed later in detail.

As mentioned above, thermal infrared images provide a spatial map of surface temperatures, and we show several examples in Fig. 2. In the upper panels, we see the mixed canopy at Harvard Forest at noontime on clear days in both winter on the left (23 January 2015, Fig. 2A) and summer on the right (1 July 2015, Fig. 2B). Here we see the importance of the data being recorded as an image: in winter, the camera is looking "through" the canopy at ground and understory, while during the summer it sees the outermost layer of the canopy. If we were using an infrared radiometer, we would have no way to tell whether the radiometer was measuring soil, understory species, branches, trunks, vegetation, or a mixture of all five at different times of the year. The lower panels show images from Niwot Ridge that are recorded five minutes apart, under different sky conditions on 30 August 2015. Fig. 2C (bottom, left) is under a cloudy sky; the canopy has settled to a uniform temperature of 21.5 °C ($\sigma = 0.2$ °C). Fig. 2D (bottom, right) is under full sun and shows how heterogeneous canopy temperature results from canopy structure ($\mu = 23.5$ °C, $\sigma = 1.2$ °C), despite air temperature remaining nearly constant during the five minute period (19.1 °C).

3.2. Image processing

All thermal images are processed in MATLAB (The MathWorks, Inc.). A custom set of functions was written to import raw image data and sensor calibration coefficients from standard FLIR .SEQ image files. Temperature outputs from these functions were then verified against the same outputs produced by FLIR's ExaminIR and ResearchIR software packages. The following concepts are valid for any thermal image, but the equation converting between temperature and sensor value is specific to the FLIR cameras we deployed. Each camera manufacturer has a different calibration algorithm, resulting in a different formula for sensor value as a function of temperature.

In our workflow, meteorological data from co-located sensors are paired with the appropriate image to correct the raw data for interference due to atmospheric conditions and thermal reflections. Subtracting the interferences yields an image of corrected, calibrated temperature.

Using Fig. 1 as a guide, we derive an expression for the total thermal energy received by the camera sensor:

$$\Phi_{tot} = \tau\varepsilon_{leaf}\Phi_{leaf} + \tau\left(1-\varepsilon_{leaf}\right)\varepsilon_{sky}\Phi_{sky} + (1-\tau)\,\Phi_{air} \tag{3}$$

Φ_{leaf} is the energy radiated by the target vegetation, while Φ_{sky} is the energy from other objects reflected off the vegetation, and Φ_{air} is the energy added by the air between vegetation and camera. ε_{leaf} and ε_{sky} are the emissivities of the vegetation and reflected objects, respectively, and τ is the transmission of the air column and accounts for attenuation of thermal signals by water vapor in the atmosphere. Higher-order reflection terms have been neglected since they involve powers of $(1-\varepsilon_{leaf})$, and therefore are small for vegetation when compared to the terms in Eq.3.

To determine vegetation temperature, we solve Eq. 3 for Φ_{leaf}:

$$\Phi_{leaf} = \frac{1}{\tau\varepsilon_{leaf}}\left(\Phi_{tot} - \tau\left(1-\varepsilon_{leaf}\right)\varepsilon_{sky}\Phi_{sky} - (1-\tau)\,\Phi_{air}\right) \tag{4}$$

The contributions of the air column and reflected objects are subtracted from the total energy received by the camera sensor. Φ_{sky} and Φ_{air} are calculated from measurements of sky temperature and air temperature using a modified version of Planck's law (Eq. 1) to convert each temperature to energy:

$$\Phi = \left(\frac{R_1}{R_2}\frac{1}{e^{\frac{B}{T}} - F}\right) - O \tag{5}$$

T is the air or sky temperature in Kelvin, B is a constant defined as $\frac{hc}{\lambda k_B}$ (see Eq. 1 for definition of constants), and R_1, R_2, F, and O are calibration constants determined by FLIR. Values for B, R_1, R_2, F, and O are embedded in the header of each thermal image recorded by a FLIR camera. Eq. 5 converts temperature to a 16-bit value that represents the energy received by the sensor. However, to complete the evaluation of Eq. 4, we also need to know the emissivities ε_{leaf} and ε_{sky}, and the atmospheric transmission in the thermal infrared, τ.

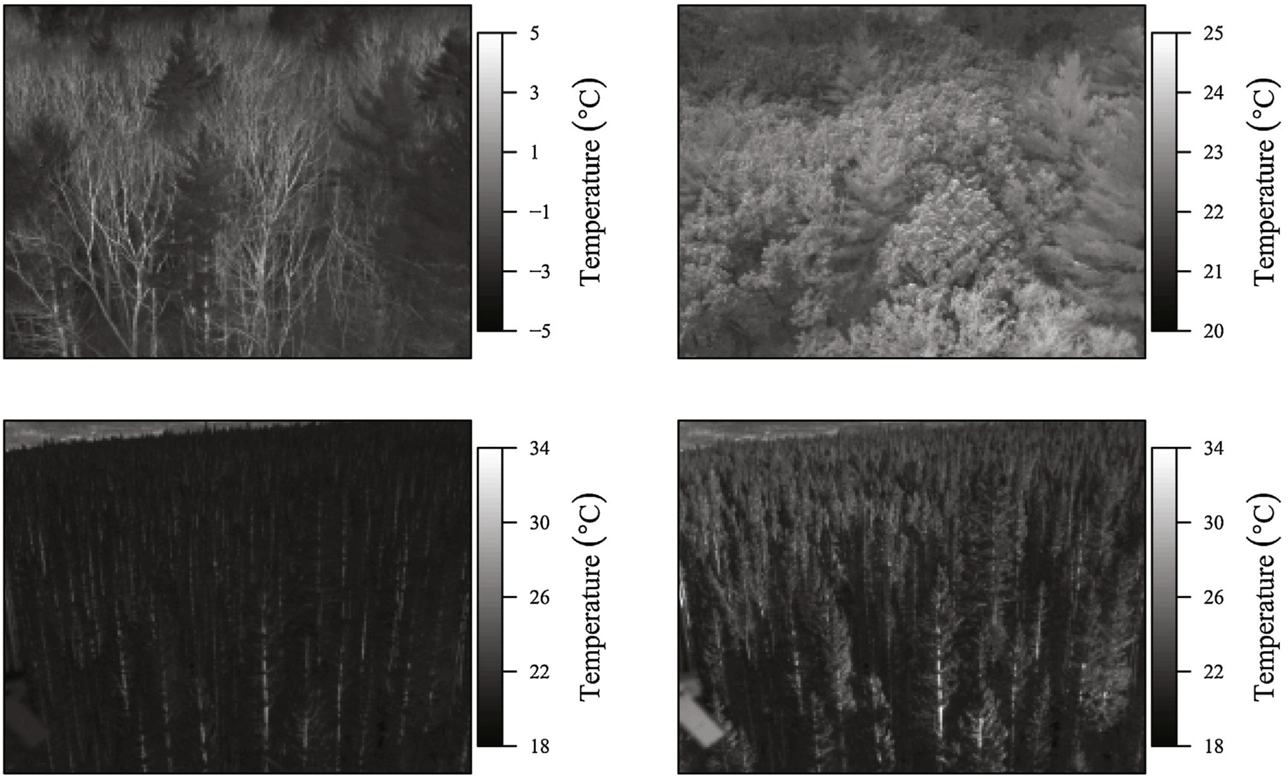

Fig. 2. Thermal images of canopy temperature patterns. White regions are warmer than black regions, and the temperature range for each image is displayed in the scale to the right. Figs. 2A,B are taken at the Harvard Forest Barn Tower and show the canopy at noontime in winter (Fig. 2A, top left) and summer (Fig. 2B, top right). Fig. 2C,D show the evergreen needleleaf canopy at Niwot Ridge under cloudy conditions (Fig. 2C, bottom left), and 5 min later under full sun (Fig. 2D, bottom right).

For this work, we assume a constant vegetation emissivity, $\varepsilon_{leaf} = 0.95$ (Grant et al., 2006; Ribeiro da Luz and Crowley, 2007; Salisbury and Milton, 1988; Ullah et al., 2012), and we assume $\varepsilon_{sky} = 1$. Transmission of thermal infrared radiation through air masses is difficult to measure in real time, and therefore must be modeled and parameterized. In the vicinity of forest canopies, the transmissive properties of air are regulated by the concentration of water vapor present. To arrive at a final transmission coefficient, we use the following equations for water vapor concentration and atmospheric transmission (Minkina and Dudzik, 2009):

$$c_{H_2O} = RH \cdot e^{\left(1.5587+6.939\times10^{-2}T_{atmC}-2.7816\times10^{-4}T_{atmC}^2+6.8455\times10^{-7}T_{atmC}^3\right)} \quad (6)$$

$$\tau = X \cdot e^{\left(-\sqrt{d}\cdot\left(\alpha_1+\beta_1\sqrt{c_{H_2O}}\right)\right)} + (1-X)\cdot e^{\left(-\sqrt{d}\cdot\left(\alpha_2+\beta_2\sqrt{c_{H_2O}}\right)\right)} \quad (7)$$

where c_{H2O} is the water vapor concentration in g/m^3, RH is the relative humidity expressed as a fraction between zero and one, T_{atmC} is the air temperature in degrees Centigrade, d is the distance between the vegetation and camera in meters, and X, α_1, α_2, β_1, and β_2 are constants determined from curve fits to LOWTRAN simulation results and are saved in the header of each image recorded by FLIR cameras. LOWTRAN is a set of radiative transfer models developed to provide accurate and rapid calculations of atmospheric transmittance at 20 cm^{-1} resolution over a broad spectral range (Kneizys, 1978). The constants X, α_1, α_2, β_1, and β_2 are unique to the algorithm FLIR has chosen for calculating attenuation by the atmosphere (Minkina and Dudzik, 2009).

Once Φ_{leaf} has been calculated, it can be substituted into the following equation to determine a corrected, calibrated temperature:

$$T_{leaf} = \frac{B}{\ln\left(\frac{R_1}{R_2(\Phi_{leaf}+O)}+F\right)} \quad (8)$$

The constants B, R_1, R_2, F, and O are the same as described in Eq. 5. This series of calculations is performed for every pixel in the image: in this way, a raw data image is converted to a calibrated, corrected temperature image.

Once the calibrated, corrected temperature image is produced, we aggregate pixels enclosed by a region of interest (ROI) and calculate the mean temperature for the ROI. ROIs are selected by hand using the guidelines developed for the PhenoCam network (Richardson et al., 2013). In short, we draw a polygon around a canopy of interest, ensuring that the sides of the polygon are several pixels inside of the canopy boundary and exclude any major gaps or woody tissues. In this manner, the ROI mean temperature is relatively insensitive to motion of the canopy from image to image, provided that the ROI has been chosen to include leaves with similar view factors. This technique is adequate for any small region that doesn't translate more than a couple pixels in the image FOV.

4. Results

4.1. Temperature sensitivity to vegetation and environmental parameters

Plots of the absolute magnitude of error in calculated temperature are shown in Fig. 3 for the warm test image (10–30 °C). These plots show error relative to the temperature calculated using the true condition parameters. The colour scale is capped at 5 °C to ensure that small errors remain visible. Plots of additional surfaces are included in Supplementary Figs. S2–S4.

Fig. 3A shows a coloured surface plot of error attributed to air temperature and relative humidity, with emissivity, distance, and reflected temperature held at their true values. The white point indicates the true value of air temperature and relative humidity at the time the image was recorded. Error is small over a wide range

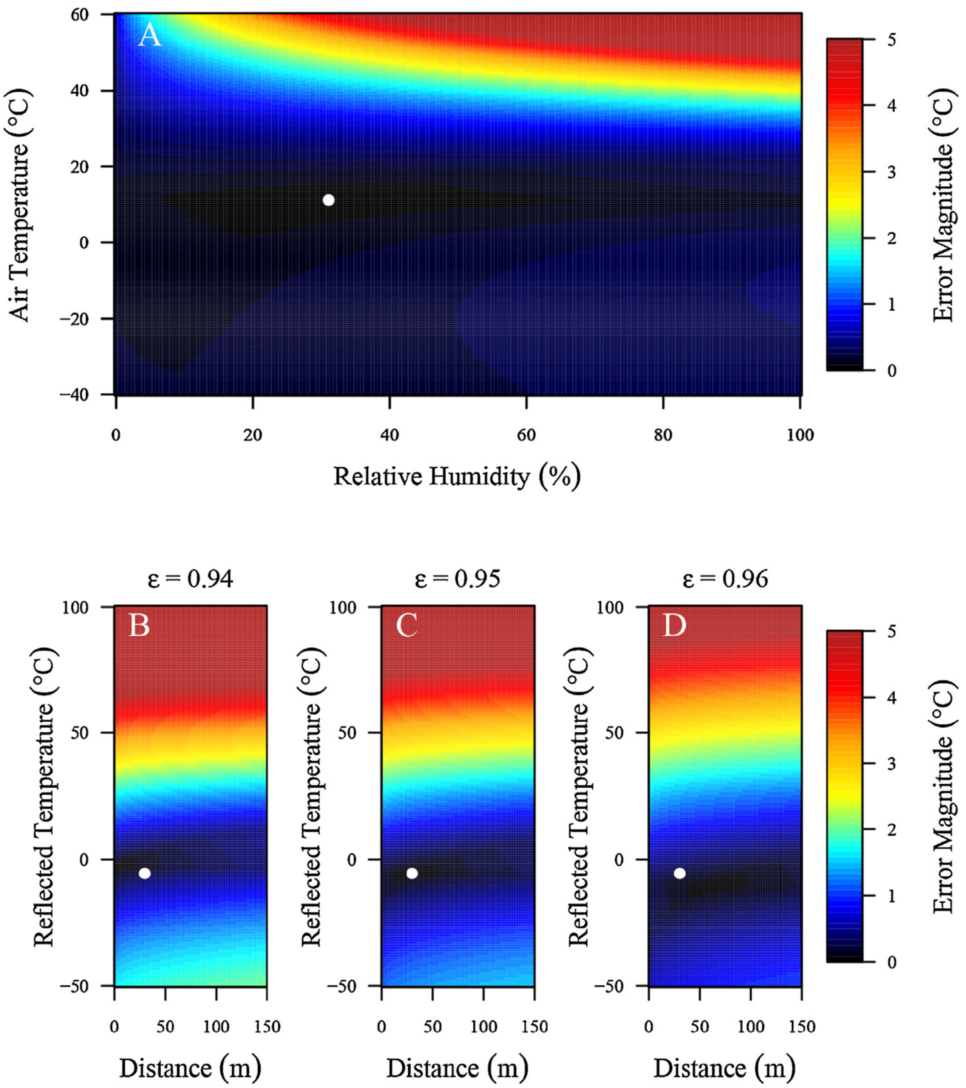

Fig. 3. Surface plots illustrate the sensitivity of corrected crown temperature to surface properties and meteorology. Fig. 3A shows magnitude of error in the corrected temperature as a function of air temperature and relative humidity, with emissivity, distance, and reflected object temperature held constant at their true values. Fig. 3B–D illustrate that small changes in surface emissivity result in large shifts in the error associated with reflected thermal energy. White points indicate true values when the image was taken.

of air temperature and humidity. Importantly, over the range of air temperature relevant to most forests (−20 to +30 °C), the errors are less than 1 °C, regardless of humidity. So long as we know emissivity, distance, and reflected temperature accurately, the accuracy of air temperature and relative humidity measurements does not need to be extremely high for us to minimize error in the calculated target object temperature.

Fig. 3B–D shows error attributed to slight differences in emissivity. The center panel shows how the error varies as a function of object distance and the temperature of reflected objects, with air temperature and humidity held at their true values. The outer panels show how the error changes for the same ranges of distance and reflected temperature at true emissivity +/−0.01. Again, the white point indicates the true value of object distance and reflected temperature at the time the image was recorded. For a given emissivity and reflected temperature, error is reasonably constant for all distances, and for a given emissivity and distance, error becomes appreciable only at reflected temperatures that are unlikely to be experienced in a forest. Error depends more strongly on emissivity than any other parameter, since a minute change in the emissivity value results in a very perceptible change in the error plot. In many regions of the plot, the change in emissivity from 0.95 to 0.94 or 0.96 (~1%, which is reasonable for vegetation) results in roughly 1 °C error, which is greater than the error range across the span of the other parameters.

Fig. S5 further illustrate the magnitude of errors associated with emissivity, showing the effect of different assumed emissivities on noontime and midnight canopy temperatures. All other environmental parameters are held fixed at their measured values, and the scatter of points in the plot is due simply to calculating canopy temperature using different values of emissivity. We see that even a change in emissivity of 0.01 (orange and green points), can result in 0.3 °C error. The magnitude of the error depends on the relative magnitude of the leaf signal compared to the air and reflected signals (Eq. 3).

4.2. Camera sensor noise

Spatial and temporal frequency analysis is performed on uniform images to ensure that signals we observe in image sequences are due to changes in the target object temperature and not simply

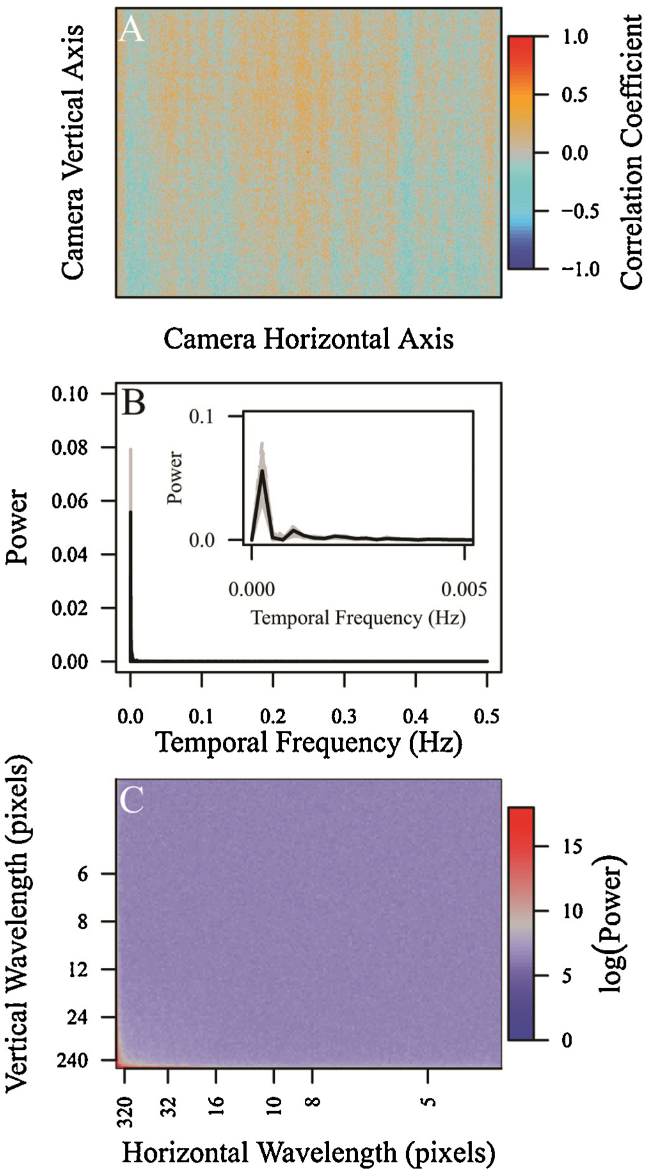

Fig. 4. Spatial and temporal analysis of noise in the TIR sensor. Fig. 4A plots the correlation coefficient between the timetrace for each pixel compared to the center pixel. Fig. 4B shows the power spectrum of temporal frequencies. The black line is the mean spectrum of all pixels, while the gray lines are 100 randomly selected pixels. Fig. 4C is a scaled image showing the two-dimensional power spectrum for spatial wavelengths. The colour scale for Fig. 4C is logarithmic.

due to noise in the sensor. Data from these analyses are presented in Fig. 4.

Fig. 4A shows the map of correlation coefficients between each pixel and the center pixel. All pixels across the sensor show correlation coefficients between −0.5 and 0.5, with minimal vertical band patterns appearing in the correlation coefficient plot. While these patterns indicate similar noise responses of pixels in a column, the coefficients remain small and hence, the sensor noise is not strongly correlated between neighboring pixels.

Fig. 4B illustrates the temporal response of pixels in the TIR sensor. We see that only low frequency components (less than 0.02 Hz) contribute appreciable power to the signal, indicating that noise fluctuates on the timescale of minutes, but that there are no rapid (timescale of seconds) signals erroneously introduced by the sensor. In fact, the low frequency components are likely an artifact of our experimental setup, since the water-filled can was not temperature controlled and its temperature slowly fluctuated by 0.8 °C through the duration of the image sequence. By subtracting off the mean of each pixel, we removed some, but not all, of the slow temperature drift and the frequency analysis analyzed the drift remaining in the signal.

Fig. 4C shows the mean two-dimensional spatial wavelength power spectrum for the sensor. The lower left corner corresponds to the DC signal (i.e. mean image temperature), which has been subtracted off, eliminating that contribution to the power spectrum. Each axis of the plot increases in spatial frequency headed away from the origin (increasing frequency = decreasing wavelength), so patterns that span large number of pixels show up near the lower left, while patterns that are only a few pixels in size show up near the far corners. Points that are not along either axis represent spatial patterns that are not aligned with the axes of the image. For example, an image composed of wide diagonal black and white lines would have a peak in the power spectrum plot that lies near the origin (distance away defined by the wavelength of the lines), but not on either axis.

In Fig. 4C, only points in the lower left corner, along the axes show appreciable power. The rest of the plot is uniformly colored: this means there are spatial patterns in the sensor noise, but the patterns are oriented along the rows and columns of pixels and span tens to hundreds of pixels. This is supported by Fig. 4A, where vertical bands appear in the correlation coefficient image. From Fig. 4C, we deduce that all off-axis directions and high spatial frequencies contribute minimal power to the images, again indicating there is little correlation between neighboring pixels caused by noise.

4.3. *Camera accuracy*

As noted in the site description, we deployed a thermal reference plate and affixed fine wire thermocouples to leaves within the FOV of the cameras. We plot the temperature of the plate and leaves as recorded by camera images versus thermocouples in Fig. 5.

Once the atmospheric interferences have been accounted for (mean correction = +0.41 °C, standard deviation of corrections = 0.28 °C), the camera and thermocouple temperatures agree very well for both the plate in Fig. 5A (RMSE = 0.61 °C, $\sigma = 0.60$ °C) and the leaves in Fig. 5B (RMSE = 0.46 °C). Thus, the majority of error lies within +/−1 °C. The distribution of errors for the metal plate is peaked (kurtosis = 3.7), but skewed slightly toward negative errors (skewness = −0.28), indicating that the camera has a tendency to underestimate actual surface temperatures. The timeseries of leaf temperature show that the camera and thermocouples capture the thermal dynamics of the vegetation equally well.

4.4. *Thermal patterns in deciduous canopies*

Finally, we look at the thermal signals from different regions of the forest canopy within the FOV of our camera at Harvard Forest. Since images are recorded continuously, and occasionally at very high frequency, we plot temperatures on different timescales for multiple regions of the canopy in Figs. 6 and 7.

Fig. 6A shows the seasonal trajectory of the top of a red oak crown through the year 2014. After correcting each image for atmospheric interferences, the pixels within a region of interest (ROI) corresponding to the oak crown were averaged to produce each point plotted in Fig. 6A. Error bars have been omitted for clarity, but the standard deviation of the ROI temperature for each image is greater than single pixel errors. Leaf on/off dates are derived from PhenoCam data for the same canopy (http://www.phenocam.sr.unh.edu) (Keenan et al., 2014). We see that crown temperature increases during the spring and summer, reaching a maximum in June. For each day, air temperature is a reasonable approximation to the mean canopy temperature, but the range between midnight and noon varies. A clear separation between crown noon, crown

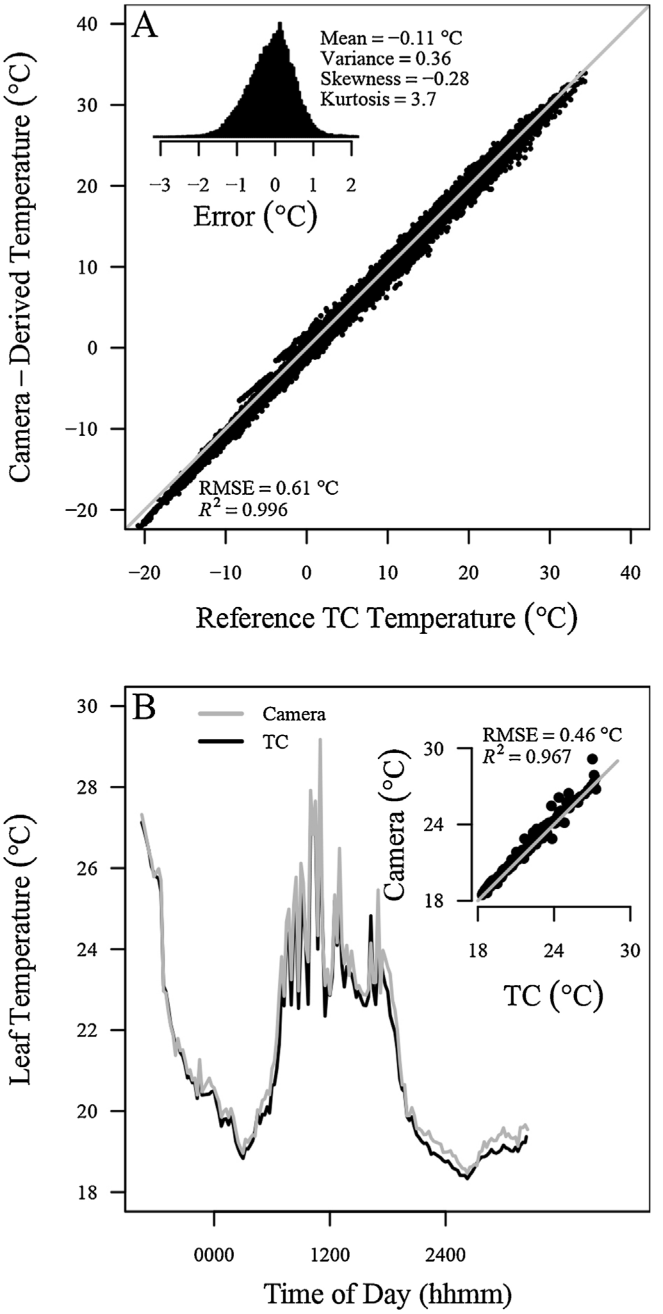

Fig. 5. Plot of temperatures recorded by thermal cameras versus thermocouples. All thermal camera data have been corrected for interferences. Fig. 5A plots temperature of the reference plate at Niwot Ridge. Each black data point is from a single image. The gray line is the 1:1 line between the axes. The inset plot shows the distribution of error in the temperatures recorded by the thermal camera ($T_{camera} - T_{thermocouple}$). Fig. 5B plots leaf temperature at Harvard Forest. The black line is the mean of twelve fine-wire themocouples affixed to oak leaves. The gray line is mean of camera pixels that encompass the oak canopy where the thermocouples were mounted. The inset plots camera-derived temperature versus thermocouple-measured temperature.

midnight, and daily mean air temperature is only present during the warmest parts of the summer. During other periods, the ranges of the three temperatures overlap more closely.

Fig. 6B plots daily temperature for two different red oak crowns on 6 May 2014. The red points are the same crown plotted in Fig. 6A, and correspond to the temperature of a crown completely surrounded by other oak and maple crowns. The blue points are from an oak crown bordering a narrow cut through the forest, such that it is exposed to mid-canopy atmospheric conditions, but receives the

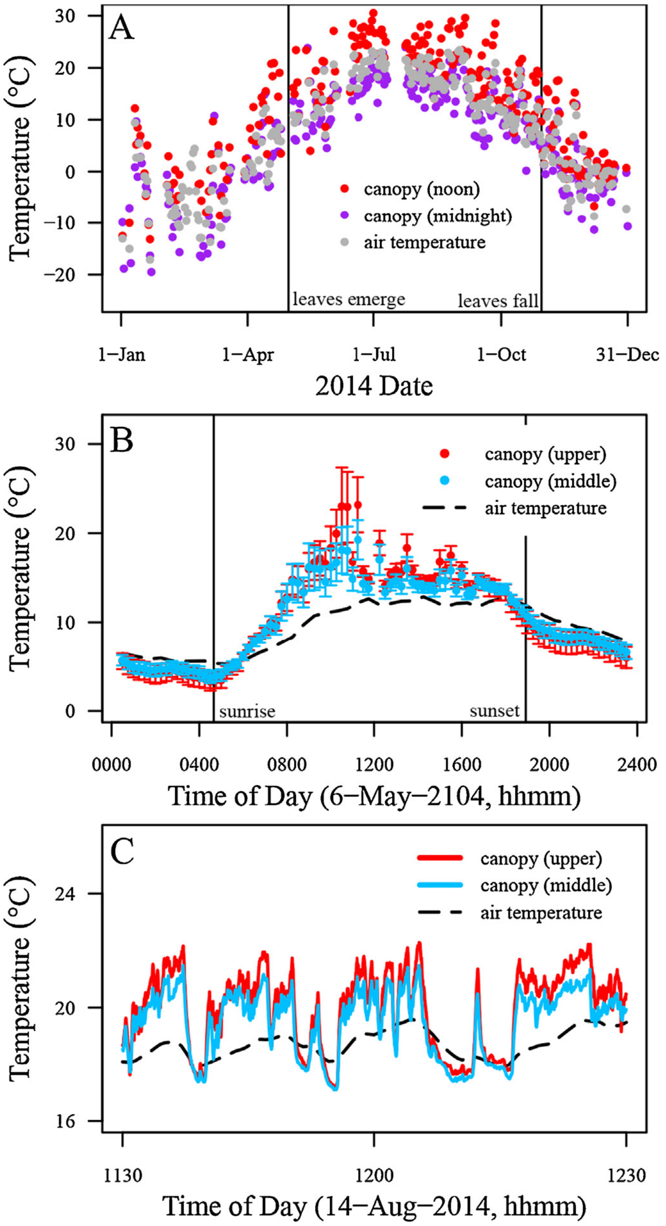

Fig. 6. Crown temperature patterns at multiple timescales. Fig. 6A plots the midnight and noon temperature of a red oak crown and compares those values to mean daily air temperature. Fig. 6B shows the temperature patterns in 15 min intervals for two red oak crowns: a crown top surrounded by other crowns (red, same as analyzed in Fig. 6A), and a crown on the forest edge (blue) (6 May 2014). Fig. 6C shows crown temperatures for the same crowns displayed in Fig. 6B, plotted at one-second intervals (14 Aug 2014). (For interpretation of the references to colour in this figure legend, the reader is referred to the web version of this article.)

same solar illumination as the first crown. Images are acquired at 15 min intervals, and error bars are the standard deviation of values across each ROI. Air temperature is plotted as 30 min means. We see that the two crowns track one another and are different from air temperature, though there is a point at late morning where the crowns decouple and show different temperature fluctuations through the afternoon, likely as the result of different local wind gusts and humidity.

Fig. 6C plots short timescale differences between the two crowns in Fig. 6B. Images for this series were acquired every second on 14 August 2014. The ROI mean for each image is plotted, and error bars are eliminated for clarity. Air temperature is plotted as the 30 s mean of inlet air temperature for the eddy covariance system on the tower, sampled at 10 Hz. We observe that the crowns are typically warmer than air temperature, exhibit strongly correlated fluctuations, and are very dynamic. The crowns change temperature by 4 °C or more every few minutes as clouds pass in front of the sun, though the upper canopy cools less during these changes. These large temperature changes are correlated between the two canopies, but there are instances of less drastic change in only one of the crowns.

Fig. 7 plots crown temperature by species for three consecutive seasons and links temperature variations to local meteorological conditions. Fig. 7A shows the greenness timeseries for the canopy in the FOV of the camera; this is the green chromatic coordinate (GCC) calculated from the Phenocam archive used for leaf on/off dates on in Fig. 6A (Keenan et al., 2014; Sonnentag et al., 2012). These data are used to demarcate the growing seasons and indicate when the thermal camera is seeing a crown of leaves or bare branches for deciduous canopies. Fig. 7B–D plot mean incident PPFD, wind speed, and air temperature for the 30 min period closest to the image analyzed each day. Fig. 7E–H plot crown temperature minus air temperature for four different species. Only the closest image to noon each day was analyzed. If no image existed for the time between 1100 and 1300 standard time each day, no data from that day is plotted. Closed circles correspond to data from sunny days, while open circles are data from cloudy days, where we define cloudy as diffuse radiation exceeding 66.67% of total incoming radiation received by the sunshine sensor during the 30 min averaging period.

A couple of patterns emerge in Fig. 7. First, the white pine (PIST) crown shows the strongest coupling to air temperature across the year. Red maple (ACRU) and red oak (QURU) show strong warming of branches immediately preceding bud burst and leaf emergence, and strong warming of foliage and branches late in the growing season. Paper birch (BEPA) is consistently warmer than air, regardless of the time of year and leaf state.

In addition, cloudy days result in crown temperatures that are much closer to air temperature, while sunny days yield crown temperatures that are elevated above air temperature. A multiple linear regression analysis between the independent variables %diffuse light, wind speed, vapor pressure deficit (VPD), and GCC, and the response variable red maple crown temperature deviation ($R^2 = 0.56$) shows that wind speed accounts for changes of −0.04 °C/(m/s) (S.E. = 0.02 °C/(m/s)), while GCC drives changes of −11.4 °C/(100% green) (SE = 1.43 °C/(100% green)), VPD drives changes of 0.47 °C/kPa (S.E. = 0.15 °C/kPa), and percent diffuse light drives changes of −3.9 °C/100% (S.E. = 0.20 °C/100%). This supports an observation from Fig. 7 that increased wind velocity does not guarantee better coupling between tree crown and air temperature, and an observation from Fig. 6C that the loss of direct solar illumination has a substantial impact on canopy temperature.

5. Discussion

5.1. Temperature sensitivity to object and environmental parameters

Thermal interferences from the atmosphere and surroundings can dramatically affect the recorded temperature of vegetation. As the plots in Fig. 3 and the supplemental information show, these interferences are multivariate and complex, making it necessary to calculate their contributions to each image. Nevertheless, it is possible to establish guidelines for the accuracy with which each variable must be recorded.

It is apparent from Fig. 3B and S5 that vegetation emissivity has a very strong impact on the magnitude of error in corrected temperatures. Since emissivity appears in each term of Eq. 4, small changes in emissivity have impacts on the partitioning of detected radiation between the sources indicated in Fig. 1. It is of paramount importance that the surface emissivity be accurately known for vegetation imaged by a TIR camera. While emissivity values can be drawn from literature, it is best to measure representative vegetation. However, the size of individual leaves relative to camera pixels must be considered before blindly applying an emissivity. As the projected image size of individual leaves becomes small relative to a pixel, the appropriate emissivity tends toward that of a blackbody radiator. This is because multiple scattering ensures that nearly all of the incoming thermal radiation is absorbed by some part of the canopy. Thus, while the emissivity value of a single leaf might be applicable to images where single leaves are comparable to or larger than a pixel, the emissivity value of a canopy image in which multiple leaves are contained within a single pixel is much closer to 0.99 (Guoquan and Zhengzhi, 1992). Assuming a representative leaf length of 10 cm, a 45° FOV, and a sensor pixel side length of 17 μm, leaves in the image become comparable to single pixels when the leaves are 40 m away from the camera. This means that leaf emissivity values should be used for the first two rows of tree crowns in the images recorded by our A655 at Harvard Forest (Fig. 2A and B), and that a blackbody value should be used for pixels on the horizon. The intermediate canopy requires an emissivity between these two values, though the mathematical details of determining that value require further attention.

Air temperature and relative humidity are easy quantities to measure. From Fig. 3A, we see that for the range of air temperatures and relative humidity likely to be experienced in a temperate or subalpine forest, thermal image temperature errors fall within +/−0.5 °C, provided that other quantities are measured accurately. This means that it is not necessary to use ultra-fast or ultra-accurate temperature and relative humidity sensors. Instrument accuracy of a couple degrees for ambient air temperature, and ten percent for relative humidity is sufficient.

The final two parameters, distance between the camera and canopy, and the temperature of reflected objects, can cause significant errors. But, these tend to be overwhelmed by incorrect emissivity or drastically incorrect air temperature and humidity. In general, for vegetation with emissivity >0.95, we find that distance accuracy of 10 m and reflected object temperature accuracy of 10 °C provides good constraint on errors in the vegetation temperature.

In general, a thermal camera deployed to the field needs to have co-located air temperature and relative humidity probes as a bare minimum. We also strongly suggest co-locating a 4-channel net radiometer to report sky temperature, though only the downwelling long-wave pyrgeometer is really necessary. A differential net long-wave signal is insufficient: signals from both the downwelling and upwelling sensors must be recorded. Sky temperature derived from sky within the FOV of the thermal camera is likely to be inaccurate, as under many sky conditions, the sky temperature is outside the calibration range of the thermal camera (clear sky ∼ −40 °C, full overcast ∼ 10 °C). It is possible to measure sky temperature using an upward-pointing single-pixel infrared radiometer, though clear sky days are again likely to fall near the edge of or even outside the calibration range.

After deploying the camera, distance to the canopy needs to be accurately measured and recorded. Analysis of crown temperatures for complex scenes, such as the FOV of our A655 cameras, will benefit from 3D canopy models to determine distance for each pixel in the image. We also recommend placing a thermal reference plate within the FOV of all cameras so that camera-derived temperatures can be verified against thermocouple temperatures for the reference. The emissivity of the reference's surface must be measured, and the response time of the reference thermocouple must be kept small to accurately report skin temperature, the quantity recorded by thermal cameras. As shown by the data in Fig. 5, following these

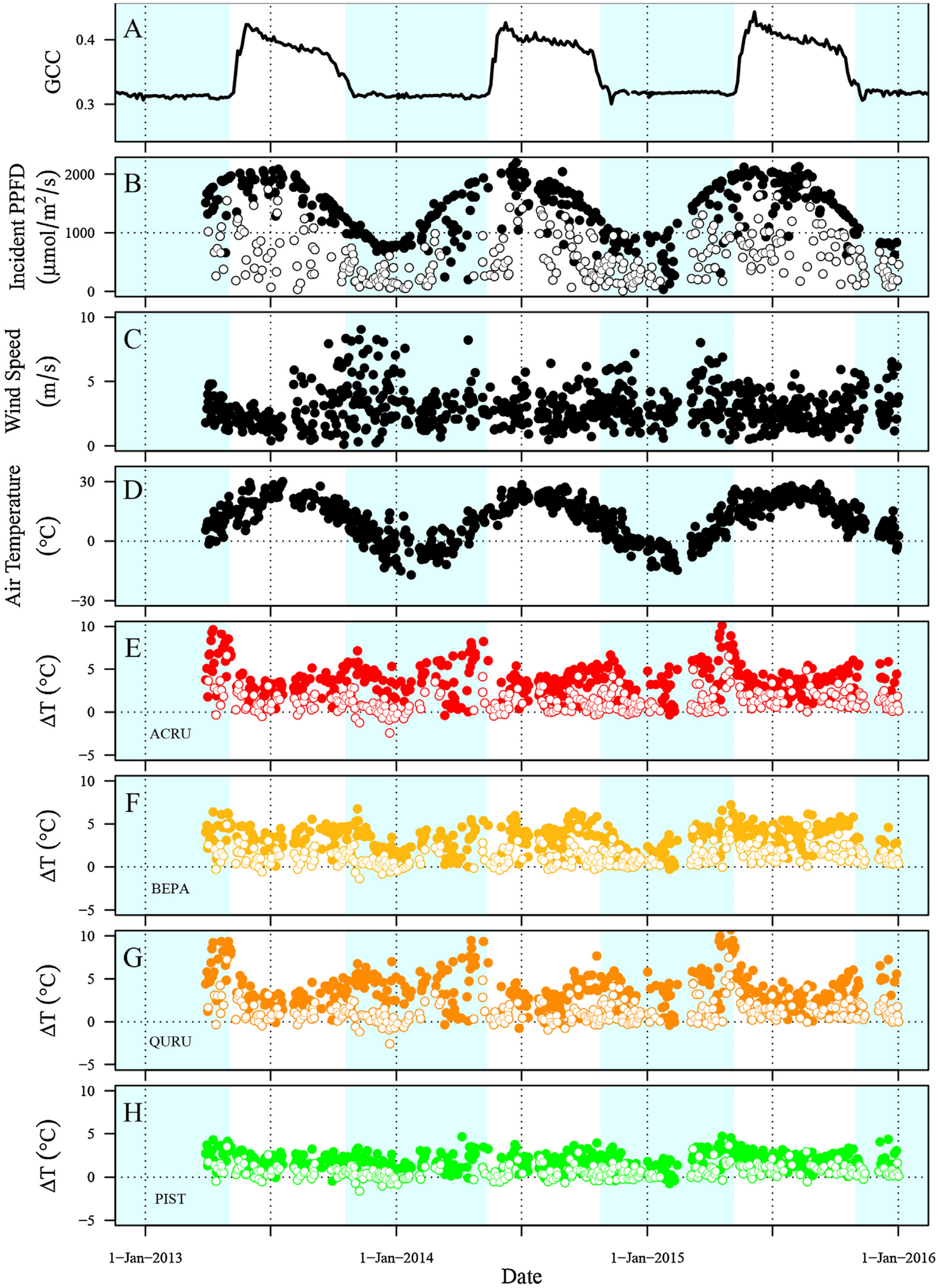

Fig. 7. Noontime crown temperature patterns across multiple seasons at Harvard Forest. Species crown temperatures are determined as region of interest averages from the image closest to noon on each day. Other measurements plotted are the 30 min mean value closest to the image acquisition time. Filled circles are sunny days, while open circle are cloudy days, as determined by a direct/diffuse sunshine sensor. Background shading indicates pheonological winter (no leaves on deciduous trees), while the white regions are the growing season. Fig. 7A plots the greenness timeseries (GCC = green chromatic coordinate) derived from Phenocam imagery of the canopy at the Barn Tower. Fig. 7 B shows incident PPFD, Fig. 7C plots wind speed, and Fig. 7D plots air temperature. Figs. 7E–H plot crown temperature deviation by species (ACRU = red maple, BEPA = paper birch, QURU = red oak, PIST = white pine), calculated as crown temperature minus air temperature. All error bars are omitted for clarity. (For interpretation of the references to colour in this figure legend, the reader is referred to the web version of this article.)

suggestions results in minimized temperature errors that are well within the range specified by the camera manufacturer, which is presumably determined indoors under "ideal" conditions.

The corrections due to thermal interferences are important, but the quality of the image data should be considered before applying any corrections. Accounting for interference will not enhance images that are out of focus or taken under conditions of low thermal contrast, for example during high humidity or precipitation. Under such conditions, it may be assumed that the scene is at uniform temperature, but the camera is only measuring the temperature of the water in the atmosphere, and it is impossible to verify the vegetation temperature. Even for good images, the error space of interference corrections is quite large, and the interplay between parameters means that the correct temperature can be arrived at using incorrect inputs. Careful checking of imaging conditions, parameter ranges, and general accuracy is more important than ultra-accurate measurements of meteorological conditions.

5.2. *Camera sensor noise*

Characterizing the sensor noise is imperative for ensuring that thermal fluctuations are attributable to the vegetation and objects within the field-of-view. By imaging a uniform object and analyzing the frequency components both temporally and spatially, along with correlations between pixels, we build constraints on the characteristics of the sensor noise.

We observe that only low frequencies contribute any appreciable amount of power to temporal signals (Fig. 4B) or spatial patterns (Fig. 4C). In addition, noise is mostly uncorrelated between pixels and there are no major spatial patterns present in the noise (Figs. 4A,C). This means that rapid temperature changes, such as those observed in Fig. 6C, are due to changes in vegetation temperature, not sensor noise. It also indicates that adjacent ROIs or pixels are unlikely to display erroneous correlation. We conclude that if signals produced from TIR timeseries are correlated, this is because the vegetation temperature is responding similarly for each ROI.

5.3. *Camera accuracy*

Thermal infrared imaging is a powerful tool for ecological studies, providing the possibility of accurate, continuous, real-time measurement of vegetation temperature. However, obtaining accurate temperature measurements requires understanding the limitations of the technology and correcting for potential interferences. FLIR's performance specifications for our cameras state that corrected temperatures are accurate to +/−2 °C or +/−2% of the reading, whichever is greater, though these values are established indoors using a precision blackbody and two point calibration.

Following correction for interferences, images taken in the field are within specification for most temperatures (Fig. 5). As the object temperature decreases, the temperature reported by the camera begins to deviate from the actual object temperature, and below −5 °C, the camera temperature is at least 1 °C colder than true temperature. Thankfully, there are few plant processes operating at these temperatures, and so we conclude that for temperatures physically-relevant to plant processes, the thermal cameras we have tested are capable of reporting temperatures within +/− 1 °C or better in real field monitoring conditions.

We attribute the remaining uncertainty in camera-derived temperatures to a mixture of random error and correctable factors: in particular, the view factor of the vegetation we are studying, and differences in response time between the TIR sensor and the thermocouples. View factor is a complicated item to address, as the sources of reflected thermal energy are unique to each point in a canopy, and vary in magnitude depending on canopy structure, surface orientation, and meteorological conditions. In light of this complicated many-body problem, we simplified the analysis by assuming that the view factor for all parts of the canopy is dominated by the sky and thus we use the sky temperature to calculate energy reflected by the canopy. Future work is needed to explore the importance of small differences and changes in view factor.

Combining our analysis of sensor noise with tests of camera accuracy, we trust that temperature differences observed in our corrected images are real temperature differences. This is true both spatially and temporally: observed temperature differences are true for two regions of the canopy at different temperatures in a single image, or for a single region of the canopy at different temperatures in two different images. Indeed, Fig. 5B demonstrates that the camera captures the temporal dynamics of vegetation with accuracy and precision equivalent to fine wire thermocouples affixed to leaves.

5.4. *Temperate forest crown temperatures*

The crown temperature plots in Figs. 6 and 7 display patterns on different timescales. On seasonal and daily timescales, crown temperature tracks the air temperature, but is usually warmer than the air during daylight hours. Canopy structure, local weather conditions, species, leaf development, and leaf physiological processes such as transpiration impact the difference between crown and air temperature.

On a daily scale, we find that crown temperature increases rapidly as soon as the sun strikes the canopy. The crown temperature overshoots air temperature by 10 °C or more, and remains elevated above air temperature until the atmosphere becomes unsettled and wind gusts begin to convectively cool the vegetation. In the evening, crowns cool rapidly due to radiative loss to the sky, and crown temperatures remain depressed below air temperature overnight. On even faster timescales, we observe both small and large temperature fluctuations in multiple regions of the canopy. The majority of the fluctuations are correlated with each other, but there are occurrences of uncorrelated signals between nearly adjacent crowns. The largest of the fluctuations shown in both Figs. 6 C and 5 B are due to patchy clouds passing in front of the sun. This removes the direct solar load from vegetation and allows the canopy to rapidly cool to air temperature.

On all timescales, the magnitude and frequency of crown temperature deviation from air temperature likely affects leaf-level processes, but the impacts are not known and can now be studied. These data will be invaluable for validating and improving leaf energy balance models, and by extension, for improving estimates of the variation in canopy conductance on diurnal and seasonal time scales.

6. Conclusions

The role of temperature in mediating plant processes underlines the importance of accurately measuring canopy temperature at high temporal and spatial resolution. We have demonstrated that thermal infrared cameras are uniquely well suited to this task and are a tool that will help elucidate new understanding of leaf development, energy balances, evapotranspiration and water balance, and regulation of photosynthesis and the carbon cycle. The three-year data record we have collected has led us to understand the challenges and limitations, but also the enormous potential, of deploying thermal cameras for continuous, high frequency measurements of vegetation temperature in the field. Several factors contribute thermal interference to the signal recorded by the cameras, including the surface properties of vegetation and ambient environmental conditions. With careful analysis, detailed knowledge of the vegetation under study, and data from co-located instruments, these interferences can be corrected, and error in the measured vegetation temperature minimized.

The initial data we have collected for a deciduous broadleaf canopy shows features across multiple timescales. We observe both a seasonal and diurnal cycle in canopy temperature that is not solely attributable to air temperature. On faster time scales, we observe rapid temperature fluctuations in different regions of the canopy that depend on differences in canopy microclimate, leaf structure, and branch orientation. This thermal image dataset will help constrain leaf and canopy-scale models of photosynthesis, water loss, and phenology, providing the information required to test the accuracy of models that currently rely on air temperature, energy balance solutions, or satellite-derived products. Deploying additional thermal infrared cameras to other ecosystems, starting long-term archives of canopy temperature, and pairing this data to measurements from flux systems, visible and hyperspectral cameras, and ground-truth observations is key to improving our understanding of plant processes and ecosystem interactions.

Funding

This work was supported by funding from the National Science Foundation's Macrosystems Biology program (grant numbers 1241616, 1241873). Research work at Harvard Forest is also partially supported by the National Science Foundation's Long Term Ecological Research program (grant numbers DEB-0080592, DEB-1237491). The authors and the contents of this work are not affiliated with and did not receive financial support from FLIR Systems, Inc.

Acknowledgements

The authors appreciate the assistance of Jonathan Dandois in taking digital images to generate the canopy pointcloud at Harvard Forest, and the support of David R. Bowling and Sean P. Burns with instrument installation at Niwot Ridge.

Appendix A. Supplementary data

Supplementary data associated with this article can be found, in the online version, at http://dx.doi.org/10.1016/j.agrformet.2016.07.017.

References

Ballester, C., Castel, J., Jiménez-Bello, M.A., Castel, J.R., Intrigliolo, D.S., 2013. Thermographic measurement of canopy temperature is a useful tool for predicting water deficit effects on fruit weight in citrus trees. Agric. Water Manage. 122, 1–6, http://dx.doi.org/10.1016/j.agwat.2013.02.005.

Berger, B., Parent, B., Tester, M., 2010. High-throughput shoot imaging to study drought responses. J. Exp. Bot. 61, 3519–3528, http://dx.doi.org/10.1093/jxb/erq201.

Campbell, G.S., Norman, J.M., 1998. An Introduction to Environmental Biophysics, 2nd edition. Springer Science+Business Media, LLC, New York, NY.

Dandois, J.P., 2014. Remote Sensing of Vegetation Structure Using Computer Vision PhD Thesis. University of Maryland, Baltimore County.

Gates, D.M., 1964. Leaf temperature and transpiration. Agric. Meteorol. 56, 273–277.

Gates, D.M., 1968. Transpiration and leaf temperature. Annu. Rev. Plant Physiol. 19, 211–238.

Gates, D.M., 1980. Biophysical Ecology. Springer-Verlag, New York, NY.

Gonzalez, R.C., Woods, R.E., Eddins, S.L., 2009. Digital Image Processing Using MATLAB, 2nd edition. Gatesmark Publishing.

Grant, O.M., Chaves, M.M., Jones, H.G., 2006. Optimizing thermal imaging as a technique for detecting stomatal closure induced by drought stress under greenhouse conditions. Physiol. Plant. 127, 507–518, http://dx.doi.org/10.1111/j.1399-3054.2006.00686.x.

Guoquan, D., Zhengzhi, L., 1992. The apparent emissivity of vegetation canopies. Int. J. Remote Sens. 14, 183–188, http://dx.doi.org/10.1080/01431169308904329.

Jensen, J.R., 2000. Remote Sensing of the Environment: An Earth Resource Perspective, 1st edition. Inc. Prentice-Hall, Upper Saddle River, NJ.

Jones, H.G., Serraj, R., Loveys, B.R., Xiong, L., Wheaton, A., Price, A.H., 2009. Thermal infrared imaging of crop canopies for the remote diagnosis and quantification of plant responses to water stress in the field. Funct. Plant Biol. 36, 978–989, http://dx.doi.org/10.1071/FP09123.

Jones, H.G., 1999. Use of thermography for quantitative studies of spatial and temporal variation of stomatal conductance over leaf surfaces. Plant. Cell Environ. 22, 1043–1055, http://dx.doi.org/10.1046/j.1365-3040.1999.00468.x.

Jones, H.G., 2004. Application of thermal imaging and infrared sensing in plant physiology and ecophysiology. In: Callow, J.A. (Ed.), Advances in Botanical Research: Incorporating Advances in Plant Pathology. Elsevier Academic Press, San Diego, CA, pp. 107–163.

Keenan, T.F., Darby, B., Felts, E., Sonnentag, O., Friedl, M., Hufkens, K., O' Keefe, J.F., Klosterman, S., Munger, J.W., Toomey, M., Richardson, A.D., 2014. Tracking forest phenology and seasonal physiology using digital repeat photography: a critical assessment. Ecol. Appl. 24, 1478–1489, http://dx.doi.org/10.1890/13-0652.1.

Kneizys, F.X., 1978. Atmospheric transmittance and radiance: the LOWTRAN code. In: 1978 Technical Symposium East. International Society for Optics and Photonics, pp. 6–8.

Semiconductors and semimetals Kruse, P.W., Skatrud, D.D. (Eds.), 1997. Uncooled Infrared Imaging Arrays and Systems, vol. 47. Academic Press Limited, San Diego, CA.

Kusse, B., Westwig, E., 1998. Mathematical Physics: Applied Mathematics for Scientists and Engineers. John Wiley & Sons, Inc, New York.

Lambers, H., Chapin III, F.S., Pons, T., 1998. Plant Physiological Ecology. Springer-Verlag, New York, http://dx.doi.org/10.1007/978-1-4757-2855-2_2.

Leuzinger, S., Körner, C., 2007. Tree species diversity affects canopy leaf temperatures in a mature temperate forest. Agric. For. Meteorol. 146, 29–37, http://dx.doi.org/10.1016/j.agrformet.2007.05.007.

Leuzinger, S., Vogt, R., Körner, C., 2010. Tree surface temperature in an urban environment. Agric. For. Meteorol. 150, 56–62, http://dx.doi.org/10.1016/j.agrformet.2009.08.006.

Long, S.P., Woodward, F.I. (Eds.), 1988. The Society for Experimental Biology, Cambridge.

Miller, P.C., 1971. Sampling to estimate mean leaf temperatures and transpiration rates in vegetation canopies. Ecology 52, 885–889.

Miller, P.C., 1972. Bioclimate, leaf temperature, and primary production in red mangrove canopies in south florida. Ecology 53, 22–45.

Minkina, W., Dudzik, S., 2009. Infrared Thermography: Errors and Uncertainties. John Wiley & Sons, Ltd, Chichester, UK.

Reinert, S., Bögelein, R., Thomas, F.M., 2012. Use of thermal imaging to determine leaf conductance along a canopy gradient in European beech (Fagus sylvatica). Tree Physiol. 32, 294–302, http://dx.doi.org/10.1093/treephys/tps017.

Ribeiro da Luz, B., Crowley, J.K., 2007. Spectral reflectance and emissivity features of broad leaf plants: prospects for remote sensing in the thermal infrared (8 0–14.0 (m). Remote Sens. Environ. 109, 393–405, http://dx.doi.org/10.1016/j.rse.2007.01.008.

Richardson, A.D., Klosterman, S., Toomey, M., 2013. Near-surface sensor-derived phenology. In: Schwartz, M.D. (Ed.), Phenology: An Integrative Environmental Science. Springer, Netherlands, pp. 413–430, http://dx.doi.org/10.1007/978-94-007-6925-0.

Salisbury, J.W., Milton, N.M., 1988. Thermal Infrared (2: 5–13. 5 μm) Direction Hemispherical Reflectance of Leaves. Photogramm. Eng. Remote Sens. 54, 1301–1304.

Scherrer, D., Bader, M.K.-F., Körner, C., 2011. Drought-sensitivity ranking of deciduous tree species based on thermal imaging of forest canopies. Agric. For. Meteorol. 151, 1632–1640, http://dx.doi.org/10.1016/j.agrformet.2011.06.019.

Schimper, A.F., 1903. Plant-geography upon a Physiological Basis. Clarendon Press, Oxford.

Sonnentag, O., Hufkens, K., Teshera-Sterne, C., Young, A.M., Friedl, M., Braswell, B.H., Milliman, T., O'Keefe, J., Richardson, A.D., 2012. Digital repeat photography for phenological research in forest ecosystems. Agric. For. Meteorol. 152, 159–177, http://dx.doi.org/10.1016/j.agrformet.2011.09.009.

Ullah, S., Schlerf, M., Skidmore, A.K., Hecker, C., 2012. Identifying plant species using mid-wave infrared (2.5–6 μm) and thermal infrared (8–14 μm) emissivity spectra. Remote Sens. Environ. 118, 95–102, http://dx.doi.org/10.1016/j.rse.2011.11.008.

Vollmer, M., Möllmann, K.-P., 2010. Infrared Thermal Imaging: Fundamentals, Research, and Applications. Wiley-VCH Verlag GmbH & Co, Weinheim, Germany.

von Humboldt, A., Bonpland, A., 1807. Essai Sur La géographie Des Plantes Accompagné d'un Tableau Physique Des Regions équinoxiales. Schoell, Paris.

Walter, H., Harnickell, E., Mueller-Dombois, D., 1975. Climate-Diagram Maps of the Individual Continents and the Ecological Climatic Regions of the Earth. Springer-Verlag, Berlin.